Macromolecules **2008**, *41*, 5441−5450

Effect of Particle Distribution on Morphological and Mechanical Properties of Filled Hydrogel Composites

Masaki Yanagioka and Curtis W. Frank*

Department of Chemical Engineering, Stanford University, Stanford, California 94305-5025

Received February 19, 2008; Revised Manuscript Received April 18, 2008

ABSTRACT: Agglomeration of particles in composite polymeric materials is a fundamental issue, but the relationship between the particle distribution and the composite mechanical properties is not fully understood. The ultimate goal of this study is to evaluate the effect of particle agglomeration upon mechanical properties of the composite. To achieve this goal, a colloidal crystalline array was encapsulated within a polymer matrix to make a model composite that has a well-ordered particle distribution. We characterized the particle distribution within the polymer matrix experimentally using Bragg diffraction of visible light and compared it with the interaction potential calculated by the Derjaguin–Landau–Verwey–Overbeek theory. Then, apparent cross-link densities of the composites were characterized from both swelling and mechanical measurements. Finally, the dynamic mechanical behavior of the composites with different particle distributions was analyzed. These data suggest that the particle distribution in the polymeric matrix plays an important role in the composite mechanical properties.

1. Introduction

Incorporation of nanoparticles into polymeric materials reinforces the mechanical properties of the composite. For example, the rubber industry has used nanoparticles as fillers to increase the mechanical strength of rubber composites for nearly a century.[1,2] A fundamental issue related to the filled composite is agglomeration of nanoparticles within the matrix polymer. This leads to a formation of a flaw, which may result in mechanical failure. The degree of agglomeration of particles, or the particle distribution in the matrix, plays an important role in mechanical properties of particle-filled composites.[3] However, understanding the relationship between the particle distribution and the composite mechanical properties is still in its infancy. The ultimate goal of this study is to understand this relationship.

To achieve this goal, there are at least two challenges. The first challenge lies in the characterization of the particle distribution itself. For example, use of scanning[4] or transmission electron microscopy[5] requires that the sample be exposed to a high vacuum and to electron beam irradiation. This carries the possibility of changing the particle distribution. Small-angle neutron[6] and X-ray scattering techniques[7] are very powerful but only available at a few locations. It would be more convenient to have a simple and more accessible technique.

The second challenge lies in the coupling of the particle−matrix interaction and the particle distribution within the matrix. Changing the surface reactivity of the particles is accompanied by the change in the particle distribution itself. Even if we try to avoid this coupling by mixing the particles until they disperse uniformly in the matrix, the shearing stresses sufficient to break up particle aggregation may lead to cleavage of some of the elastomeric chains. Thus, changing only the particle distribution without altering the molecular weight of the matrix polymer and the particle−matrix interaction is a nontrivial matter.

This study has been carried out to overcome these challenges, preparing the colloidal particle systems in such a way as to obtain different particle distributions without changing either the matrix property or the particle−matrix interactions. As a model of a relatively well-ordered particle distribution, we chose a mesoscopically periodic colloidal crystalline array (CCA) of spherical colloids.[8] The CCA is known to self-assemble due to electrostatic repulsion into a minimum-energy configuration. This material comprises a body-centered cubic (BCC) or face-centered cubic (FCC) array of spherical particles.[9] Because the interparticle distance in the CCA is comparable to visible wavelengths, samples exhibit iridescence due to the diffraction of visible light and, thus, meet the Bragg condition. This length scale of the interparticle distance enables us to characterize it by scanning only the visible wavelength of the diffracted light.[10–13]

However, the CCA will disorder upon mechanical shock and/or introduction of ionic impurities, which screen the interparticle repulsive interactions.[8] To counteract this, Asher et al.[10–12] have developed an approach to lock in the CCA ordering by embedding the arrays in a cross-linked polymeric matrix; they called this composite system polymerized CCA (PCCA). In particular, Asher et al. introduced nonionic monomers into the CCA that can form a hydrogel network, yielding a PCCA hydrogel composite that locks in the crystal structure and remains stable during polymerization. The polymerization and cross-linking result in only modest changes in the CCA ordering, as evidenced by the small alterations of the diffraction peak.[13] Measuring the diffraction peak easily provides the interparticle distance, which is associated with the degree of dispersion in the matrix. Thus, use of UV−vis absorption solves the first problem of how to characterize the particle distribution; it is readily available and can be used on a wide range of samples without radiation degradation. Moreover, in the PCCA, the interparticle distance depends only upon the electrostatic repulsion. Therefore, variable particle dispersion may be achieved just by changing the electrolyte concentration. This solves the second problem and enables us to change the particle distribution without any effect upon other factors, such as the molecular weight of the matrix polymer and the matrix−particle interaction.

In principle, any nonionic monomer can be used to encapsulate the CCA. Asher et al.[10] used poly(*N*-isopropylacrylamide) (pNIPAAm) as a matrix polymer to utilize its temperature-induced volume-phase transition. This enabled the array lattice constant to vary with temperature, and the diffracted light was thermally tunable.[10] This composite system is promising and can be applied to optical switching devices. In this paper, we chose this combination of the CCA and the pNIPAAm matrix

---

* Corresponding author. E-mail: curt.frank@stanford.edu.

10.1021/ma8003778 CCC: $40.75

and will discuss the relationship between the particle distribution within the matrix and the dynamic mechanical properties of the hydrogel composite system.

2. Materials and Methods

Hydrogel Samples. The synthesis procedure of the polymerized colloidal crystalline array basically followed the work reported by Asher et al.[10–12] To prepare non-close-packed colloidal crystals immobilized in a hydrogel, an aqueous suspension containing silica spheres at 15.5 wt % having diameters of 110 nm (Nippon Shokubai Co. Ltd.) and pNIPAAm were used as the filler particle and the matrix polymer, respectively. We refer to this system as an "ordered silica-filled hydrogel" (OSHG). *N*-Isopropylacrylamide, 97% (NIPAAm, Aldrich), was recrystallized from hexane. Other chemicals were used without further purification.

The silica suspension was dialyzed against deionized water at 50 °C for 1 day (CCA-1) and 3 days (CCA-2) using a pleated dialysis tubing (MWCO = 10 000, SnakeSkin, PIERCE). It was then shaken with an excess of ion-exchange resin (Bio-Rad mixed bed, AG501-X8) until an angle-dependent iridescence was observed.

All the hydrogel composites were prepared by free-radical polymerization. First, NIPAAm monomer, *N*,*N*-methylenebis(acrylamide) (MBAAm, Sigma-Aldrich), as a cross-linker and diethoxyacetophenone (DEAP, Sigma-Aldrich) as a light-sensitive initiator were dissolved in the CCA-2 suspension. The monomer concentration was 1.1 M (12 wt %). The molar ratio of the NIPAAm monomer, cross-linker, and initiator was 100:2:0.23. Prior to dissolution, oxygen in the deionized water and the silica suspension was removed by bubbling with nitrogen gas for 20 min. The DEAP was dissolved in dimethyl sulfoxide (DMSO, Sigma-Aldrich) at 10 vol % before adding to the suspension. Addition of these chemicals disturbed the crystalline structure, but shaking the solution again with ion-exchange resin recovered the iridescence. Next, the solution was injected between two quartz plates separated by a 500 μm spacer and then exposed to UV light from a xenon lamp (40 mW/cm^2) for 90 s at room temperature. The resultant hydrogel, or the OSHG, was washed carefully with deionized water for 1 week.

For comparison, a conventional "pure hydrogel" (PHG) and a "random silica-filled hydrogel" (RSHG) were also prepared at the same concentrations of each chemical. For the RSHG, the silica suspension was used as supplied. The RSHGs at various silica concentrations (5.2, 10.4, and 15.5 wt %) were prepared and are referred to as RSHG-1, RSHG-2, and RSHG-3, respectively.

UV–vis Spectrophotometer. The transmittance spectra of the CCA suspension and the OSHG were collected using a Cary 3 UV–vis spectrophotometer (Varian, Inc.). Spectra were collected between the wavelengths of 350 and 850 nm at 25 °C. The OSHG sample was sandwiched between two quartz plates with spacers having different thicknesses in order to control the degree of compression. The UV–vis light was directed normal to the sample surface.

Zeta Potential and Conductance Measurement. The zeta potential of the silica spheres before and after dialysis was measured at pH 6 with a ZetaPlus zeta potential analyzer (Brookhaven Instruments Corp.) at 25 °C.

The counterion in the aqueous solution used in the study was the sodium ion from the sodium dodecyl sulfate. The conductance of each suspension was monitored by the same analyzer, and the calibration curve was utilized to determine the molar concentration of the counterion in the bulk solution, c_{i0}, in mol/L. The number concentration, c_{i0}* in ions/m^3, was obtained by $1000N_Ac_{i0}$, where N_A is Avogadro's number.

Swelling Experiment. Determination of the molecular weight between cross-links, $\overline{M}_c$, and the apparent cross-link density, ν_e, via swelling experiment was done by allowing the hydrogel composites (ca. 3.5 cm in diameter and 500 μm in thickness) to equilibrate in water at 25 °C.

Dynamic Mechanical Analysis. The mechanical characteristics of the PHG, RSHG, and OSHG films were determined in both shear and compression modes with an AR2000 rheometer (TA Instruments). For the shear mode, the composite samples of about 500 μm in thickness were placed on the temperature-controlled stage and the parallel plate applied shear stress. An oscillatory shear was applied at a constant strain amplitude of 10% to obtain the frequency dependence of the storage modulus, G', and loss modulus, G''. Slippage of the hydrogel from the bottom plate limited the possible frequency range. For the PHG, the accessible range was between 0.1 and 10 Hz. For the RSHG and the OSHG, the accessible range was between 0.1 and 1 Hz because the more elastic nature of these samples compared to the PHG resulted in slippage above 1 Hz. Water was added to the samples so that they were fully swollen during measurement. The temperature was varied from 5 to 25 °C. For the stress relaxation measurement, the sample was loaded to 10% shear strain and held at that strain for 300 min at 25 °C. During the relaxation period, the decrease of the stress was continuously recorded. For the compression mode, strain–stress curves for each sample at 25 °C were measured at a compression rate of 8 μm/s.

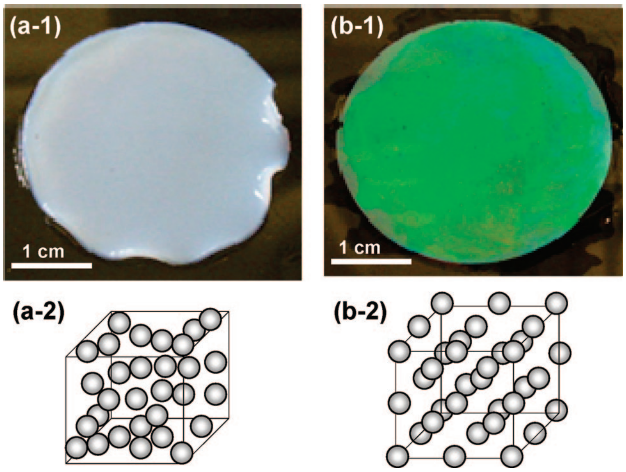

Figure 1. Photographs of (a-1) the random silica-filled hydrogel (RSHG) and (b-1) the ordered silica-filled hydrogel (OSHG), with schematics of expected particle distribution for (a-2) the RSHG and (b-2) the OSHG. Both of the samples contain silica particles (110 nm in diameter) of 15.5 wt %.

3. Results

3.1. Interparticle Distance. *3.1.1. Optical Measurement.* The appearances of the RSHG and the OSHG are shown in Figure 1. The RSHG became white due to scattering of light from randomly distributed silica particles in the hydrogel. By contrast, the OSHG exhibited brilliant angle-dependent color, with the iridescence uniformly spread over the surface of the OSHG, suggesting a homogeneous crystalline structure at the macroscopic scale.

A UV–vis spectrophotometer was utilized to determine the interparticle distance within the ordered arrays. The diffraction characteristics are sufficiently predicted through Bragg's diffraction equation:[8–13]

$$\lambda_{\text{peak}} = 2d_{hkl}n_{\text{eff}} \sin \theta \tag{1}$$

where λ_{peak} is the wavelength of the diffraction peak, d_{hkl} is the spacing between a family of lattice planes (hkl) (where h, k, and l are the Miller indices), n_{eff} is the mean effective refractive index of the sample, and θ is the angle between the incident light and the diffraction planes. In this experimental setup, where light was directed normal to the sample surface, θ was $\pi/2$. The refractive indices at each wavelength were obtained using the Cauchy equations:[14]

$$n_w = 1.324 + 3046/\lambda^2 \tag{2}$$

$$n_s = 1.458 + 3540/\lambda^2 \tag{3}$$

where λ is the wavelength of the light in nm, and n_w and n_s are the refractive indices of water and the silica nanoparticles,

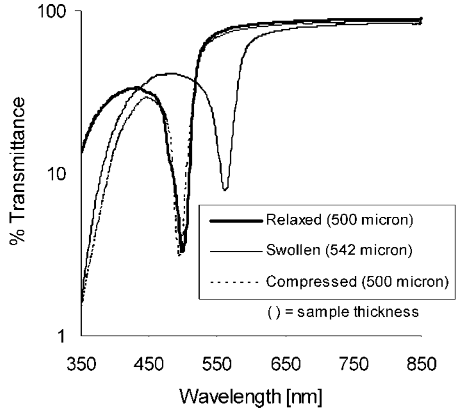

Figure 2. UV−vis spectra of the OSHG in the relaxed, swollen, and compressed states. The silica concentration in the OSHG is 15.5 wt %. Sample thicknesses are indicated in parentheses in the inset.

respectively. The refractive index of the sample was estimated as the volume-weighted average of refractive indices for water and the silica particles as follows:

$$n_{\mathrm{eff}} = n_{\mathrm{w}}(1-\phi) + n_{\mathrm{s}}\phi \qquad (4)$$

where ϕ is the volume fraction of silica in the sample.[9] For a BCC structure, the center-to-center particle separation, d, is related to the interplanar distance, d_{hkl}, via

$$d = \frac{d_{hkl}}{2}\sqrt{3(h^2+k^2+l^2)} \qquad (5)$$

$$\phi\left(\frac{d}{D}\right)^3 = 0.68 \qquad (6)$$

where D is the particle diameter and the value 0.68 is the atomic packing factor of the BCC structure or the volume fraction of spheres in contact with each other in a close-packed BCC array. For an FCC structure

$$d = \frac{d_{hkl}}{\sqrt{2}}\sqrt{h^2+k^2+l^2} \qquad (7)$$

$$\phi\left(\frac{d}{D}\right)^3 = 0.74 \qquad (8)$$

where the value 0.74 is the volume fraction of spheres in a close-packed FCC array.

Figure 2 shows the UV−vis spectrum of the OSHG, in which the sharp absorption represents the diffraction from the crystalline structure in the hydrogel. The sample in the relaxed state has a diffraction wavelength at 494 nm, which corresponds to an interplanar spacing, d_{hkl}, of 182 nm at the silica concentration of 15.5 wt %. After the OSHG was equilibrated in deionized water for 3 days, the diffraction peak red-shifted to 560 nm, which gave an interplanar spacing of 206 nm. Swelling resulted in an increase in the thickness of the OSHG from 500 to 542 μm. Then the OSHG was compressed between two quartz plates using a 500 μm spacer, and the UV−vis spectrum was again measured. Upon compression, the diffraction peak returned from 560 to 493 nm, which is essentially the same peak position as that of the relaxed state (Figure 2). This peak shift corresponds to the reduction of the interparticle distance by 12%. On the other hand, the reduction in the bulk thickness of the OSHG due to compression was 8%. These values are within our experimental error, and the degree of compression of the bulk sample corresponded to the reduction in the interplanar distance of the crystalline lattice. This suggests that the microscopic interplanar distance, d_{hkl}, is controlled by the macroscopic compression of the bulk sample and that it is determined easily by UV−vis spectroscopy even though the particles are embedded in the polymeric matrix.

Table 1. Properties of Silica Aqueous Suspensions before and after Dialysis[a]

silica suspension	original	CCA-1	CCA-2
duration of dialysis (days)	0	1	3
concentration of counterion in the bulk: c_{i0} (mM)	1.25	0.16	0.08
number concentration of counterion in the bulk: c_{i0}^* (ions/m$_3$)	7.5×10^{23}	9.4×10^{22}	5.1×10^{22}
zeta potential at pH 6: Φ_0 (mV)	−24	−24	−23
Debye screening length: $1/\kappa$ (nm)	9	24	33

[a] The CCA-1 and CCA-2 suspensions experienced dialysis for 1 day and 2 days, respectively.

3.1.2. DLVO Theory. The Derjaguin–Landau–Verwey–Overbeek theory, which deals with the balance of the electrostatic repulsive interaction and the van der Waals attractive interaction, provides the classical explanation for the stability of colloids in suspension.[15a] The total interaction potential is given by a simple summation of these two opposing interactions. In this study, we made use of DLVO theory to describe the colloidal stability as well as the interparticle distance in the OSHG, based upon previous studies that demonstrate the interparticle distance is determined in the suspension and is fixed upon polymerization.[13]

The total interaction energy $V_{\mathrm{T}}(h)$ between two particles as a function of their separation h is

$$V_{\mathrm{T}}(h) = V_{\mathrm{att}}(h) + V_{\mathrm{rep}}(h) \qquad (9)$$

where $V_{\mathrm{att}}(h)$ and $V_{\mathrm{rep}}(h)$ are the attractive and repulsive interaction potential energies as a function of their separation h, respectively. The interaction between multiple charged particles in a polar medium can be determined by the linear superposition approximation.[16] The requirement for this approximation is the rapid decrease of the potential from the particle surface, so that many-body effects are neglected and the interaction potential is given by linearly superposing the potentials from each particle. In this case, the potential energy at the midpoint between surfaces, $\Phi_{1/2}$, should be much smaller than the thermal energy, that is, $ze\Phi_{1/2} \ll kT$.

When this assumption holds true, the total interaction energy for two spherical particles of radius R_{p} is given as follows:

$$V_{\mathrm{T}}(h) = -\pi R_{\mathrm{p}}\frac{H_{121}}{12\pi}\frac{1}{h} + \pi R_{\mathrm{p}}\frac{64c_{i0}^{*}kT\Gamma_0^{\;2}\exp(-\kappa h)}{\kappa^2} \qquad (10)$$

$$\Gamma_0 = \frac{\exp(ze\Phi_0/2kT) - 1}{\exp(ze\Phi_0/2kT) + 1} \qquad (11)$$

where H_{121} is the Hamaker constant that is specific to the material of the surface, k is the Boltzmann constant, T is the temperature, ε_0 is the electrical permittivity of vacuum, ε_{r} is the dielectric constant of the medium, z_i is the valence of ionic species i, e is the electronic charge, Φ_0 is the surface potential of particles, and c_{i0}^* is the number concentration of the counterion species in the bulk. The Debye screening length, $1/\kappa$, represents the decay length of the surface potential or a thickness of the double layer varying inversely proportional to the square root of the bulk counterion concentration, c_{i0}^*, as

$$\frac{1}{\kappa} = \left\{\frac{\varepsilon_{\mathrm{r}}\varepsilon_0 kT}{\sum_i (z_i e)^2 c_{i0}^*}\right\}^{1/2} \qquad (12)$$

In order to determine the total interaction potential $V_{\mathrm{T}}(h)$, we need to know Φ_0 and c_{i0}^*. In fact, since the surface potential Φ_0 is difficult to measure directly, it is common to replace Φ_0 by the zeta potential.[15a] Table 1 shows the zeta potential and the Debye screening length before and after removing excess

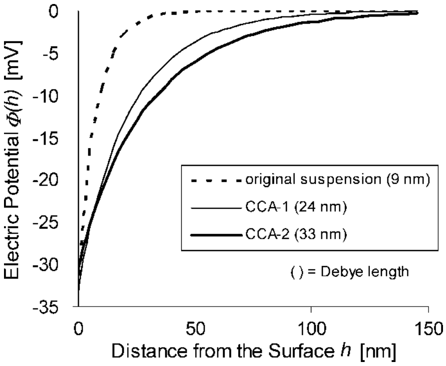

Figure 3. Electric potential curves using the equation in ref 15b as a function of distance from the silica surface for the original suspension and the CCA suspensions with different counterion concentrations. Debye screening lengths are indicated in parentheses in the inset.

ions. Dialysis and the ion-exchange resin reduced c_{i0}^* but did not have an effect on the zeta potential of the silica particles. The Debye screening length, however, increased as c_{i0}^* decreased. The removal of ions increased the Debye length by almost 3-fold for the CCA-2, and the repulsive interaction potential was changed accordingly.

Solving the Poisson−Boltzmann equation gives the change in electric potential with the distance from the charged surface.[15b] To demonstrate the effect of the removal of ions, changes in the electric potential Φ as a function of distance h from the particle surface are calculated on the basis of ref 15b and shown in Figure 3. The potential curve for the original suspension is compared with the ones for the CCAs at different c_{i0}. The magnitude of the electric potential decreases as the distance from the surface increases, and it approaches zero at long separation distance, regardless of the magnitude of c_{i0}. The CCA-2 suspension has a longer Debye length than the original suspension and the CCA-1 sample. This is caused by the larger electrostatic force at reduced c_{i0} and the thicker Debye layer.

Using these Debye lengths, we calculated the total interaction potential energy curves for the original silica suspension and the CCA-2 suspension from eq 10 (Figure 4). The reduced c_{i0} changed the interaction potentials significantly. The original suspension has a small barrier height of around 1.5kT and is quite likely to form aggregates. On the other hand, the CCA-2 has about 4-fold higher barrier height, which makes the particles repel each other. The position of the secondary minimum provides the distance from the surfaces, and it increased from 25 nm in the original suspension to 110 nm upon reduction of c_{i0} in CCA-2.

3.2. Apparent Cross-Link Density. The molecular weight between cross-links, $\overline{M}_c$, was determined by both swelling and mechanical measurements. The former was obtained by following the work reported by Bray and Merrill.[17] The equation for $\overline{M}_c$ is as follows:

$$\frac{1}{\overline{M}_c} = \frac{2}{\overline{M}_n} - \frac{\frac{\overline{\nu}}{V_1}[\ln(1-\nu_{2,s}) + \nu_{2,s} + \chi\nu_{2,s}{}^2]}{\nu_{2,r}\left[\left(\frac{\nu_{2,s}}{\nu_{2,r}}\right)^{1/3} - \frac{1}{2}\left(\frac{\nu_{2,s}}{\nu_{2,r}}\right)\right]} \tag{13}$$

where $\overline{M}_n$ is the number-average molecular weight, $\overline{\nu}$ is the specific volume of polymer (0.896 cm^3/g for pNIPAAm), V_1 is the molar volume of water (18 cm^3/mol), $\nu_{2,s}$ is the polymer volume fraction in the swollen state, $\nu_{2,r}$ is the polymer volume fraction in the relaxed state, and χ is the Flory interaction parameter between water and pNIPAAm (0.52 at 25 °C).[18] The apparent cross-link density, ν_e, was calculated as

$$\nu_e = \frac{\rho}{\overline{M}_c} \tag{14}$$

where ρ is the density of the polymer.

In order to determine $\overline{M}_n$, the viscosity-average molecular weight $\overline{M}_v$ was measured by dilute solution viscometry,[19] and the relationship for the most probable distribution in a Θ solvent, $\overline{M}_n$:$\overline{M}_v$ = 1:1.67, was utilized.[20] This relationship is a safe assumption for the pure NIPAAm polymers in water because water at 25 °C is a Θ solvent for pNIPAAm.[21]

When silica particles were absent during polymerization, $\overline{M}_n$ was 1 200 000 g/mol. However, $\overline{M}_n$ decreased dramatically to 100 000 g/mol when silica particles were added to the system before polymerization. A reduction in the molecular weight for a radical polymerization of polystyrene in the presence of silica particles was also observed by Tsubokawa et al.[22] They suggested that, during the polymerization, chain transfer of growing polymer radicals to the silica surface produced siloxyl radicals. These radicals are less stable than the radicals on the growing chain; therefore, they can be easily quenched. It is quite reasonable that this radical transfer also occurred in our system, causing a decrease in the molecular weight in the presence of silica particles.

Mechanical determination of the ν_e was achieved by essentially following methods described in previous reports.[23,24] When the sample is compressed, strain, ε, is defined as

$$\varepsilon = \lambda^{-2} - \lambda \tag{15}$$

$$\lambda = L/L_0 \tag{16}$$

where λ is the uniaxial compression ratio, L is the thickness of the sample after compression, and L_0 is the initial thickness. It was then converted to ν_e from the slope of linear dependence

$$\sigma = E\varepsilon = RT(\phi_{p,0}/\phi_p)^{2/3}\phi_p\nu_e\varepsilon \tag{17}$$

where σ is the stress, E is the elastic modulus, $\phi_{p,0}$ is the polymer volume fraction of the gel in the relaxed state, and ϕ_p is the polymer volume fraction of the gel in the swollen state.

The apparent cross-link densities from the swelling measurement for the RSHG and the OSHG were calculated and are shown as a function of silica content in Figure 5, where they are compared with the ones obtained from the mechanical measurement. In contrast to little difference in the ν_e determined in the swelling experiments, there was a significant difference between the two composites for the mechanical measurement.

Figure 6 shows the stress−strain curves at 25 °C. The experimental data obtained up to about 15% of deformation, or $\lambda^{-2} - \lambda = 0.5$, were ignored because the surface of the samples were not completely compressed by the plate and the experimental artifact is thought to be large below this point. From the slope of the straight line, the E and ν_e values were calculated and are shown in Table 2. The E and ν_e values for the PHG and all the RSHG samples were almost identical within experimental error. It should be noted, however, that the OSHG exhibited much higher E and ν_e than other samples.

In Figure 5, we observed that the apparent cross-link density determined by the mechanical testing was much higher than the one determined by the swelling method. According to Sperling,[25] the ν_e from modulus determinations is generally higher because physical cross-links tend to count more in the less-relaxed mechanical measurements than in the closer-to-equilibrium swelling data. To test whether this hypothesis holds true in our system, we decreased the compression rate for the stress−strain curves, so that the hydrogel approaches a state

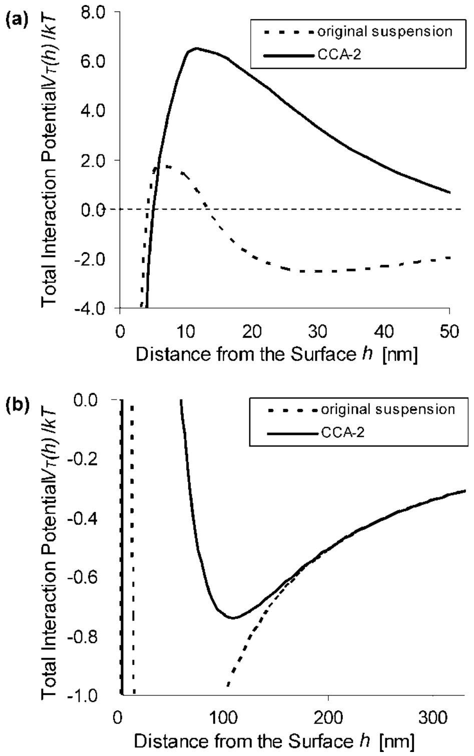

Figure 4. (a) Barrier height region and (b) secondary minimum region of the total interaction potential $V_T(h)/kT$ obtained from eq 10 for the original suspension and the CCA-2 suspension.

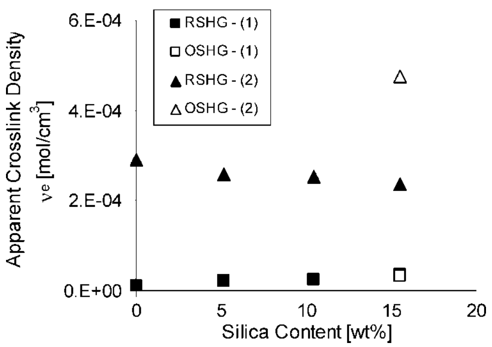

Figure 5. Apparent cross-link densities, ν_e, as a function of silica content obtained by (1) the swelling measurement and (2) the mechanical measurement.

closer to equilibrium. Figure 7 shows the ν_e for the PHG prepared with different UV polymerization times and demonstrates the effect of the compression rate for the stress−strain curve measurement. Longer UV polymerization time resulted in larger ν_e, suggesting that the polymeric network has been tightened. Slower compression rate (2 μm/s) showed lower ν_e, just as we expected. Thus, this phenomenon confirmed the hypothesis that the higher ν_e from modulus determination comes from more physical cross-links in the less-relaxed mechanical measurements.

3.3. Dynamic Mechanical Analysis. Dynamic mechanical analysis is a powerful method to investigate the properties of elastomeric substances. In order to compare the relaxation behaviors of the RSHG and the OSHG, the activation energy associated with mechanical relaxation was investigated by taking advantage of the time−temperature superposition principle (TTS).[26] TTS is based upon the premise that the processes involved in molecular relaxation or rearrangements occur at greater rates at higher temperatures. Thus, viscoelastic changes can be made to appear as if they occurred at longer times or lower frequencies simply by shifting the data with respect to time.

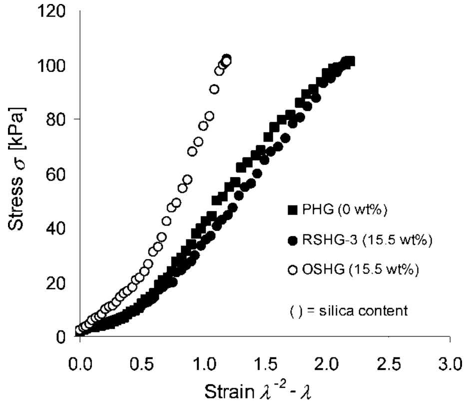

Figure 6. Stress−strain curves for the PHG, the RSHG-3, and the OSHG. Silica content is indicated in parentheses in the inset.

TTS has been applied to characterize mechanical properties of many unfilled polymer systems.[26−28] Generally, this principle does not hold for multiphase polymer blends because of the individual contributions of each phase to the rheological behavior.[29] In some cases where there is a strong interaction among the phases, however, homogeneous rheological behavior of the polymer blend has been reported.[30] The criteria for the application of TTS have been described in detail.[31] It holds when (1) the exact matching of shapes of adjacent curves is obtained, (2) the shift factor a_T has the same value for all viscoelastic functions, and (3) the temperature dependence of a_T has a reasonable form, such as given by the Arrhenius or Williams−Landel−Ferry (WLF) equations. In the following, we will examine these criteria in the context of our system and demonstrate that TTS is indeed applicable.

Of the above-mentioned two models, the Arrhenius equation directly provides the activation energy associated with mechanical relaxation, E_a. We expect that E_a should give us insight as to how the particle distribution affects the relaxation behavior of the composite; therefore, we focused on the Arrhenius dependence of the shift factor a_T to determine E_a as follows:[26]

$$\log a_T = \frac{E_a}{R}\left(\frac{1}{T} - \frac{1}{T_0}\right) \tag{18}$$

where R is the gas constant, and T and T_0 are the measurement and the reference temperature, respectively. E_a provides information on how hard it is for the material to undergo relaxation; higher E_a corresponds to a higher energy barrier to mechanical relaxation.

Figure 8a shows the storage and loss moduli of the PHG, the RSHG-3, and the OSHG as a function of frequency, with five segment curves, corresponding to the data acquired at five equally spaced isothermal steps between 5 and 25 °C. Two master curves in Figure 8b were constructed by shifting both the storage and the loss modulus curves in Figure 8a with respect to the reference temperature at 25 °C. Note that the same shift factor was applied for the storage and the loss modulus at each temperature.

For all of these samples, the storage modulus did not change as much as the loss modulus within this frequency range. Among them, the loss modulus of the PHG showed a drastic decrease (ca. 30-fold) at higher frequency. On the other hand, the loss modulus of the RSHG stayed almost constant within this frequency range. This suggests that the particle−matrix configuration of the RSHG was frozen and did not relax. This could be explained by the more elastic nature of the RSHG than the PHG because of the presence of elastic silica particles embedded

Table 2. Apparent Cross-Link Densities of the PHG, the RSHG, and the OSHG Composites Obtained from the Moduli of the Stress−Strain Curves

sample	silica distribution	silica concentration Si (wt %)	compression modulus E (kPa)	polymer volume fraction of gel in the relaxed state $\nu_{2,r}$	polymer volume fraction of gel in the swollen state $\nu_{2,s}$	apparent cross-link density ν_e (mol/cm^3)
PHG		0.0	61	0.0939	0.0703	2.9×10^{-7}
RSHG-1	random	5.2	61	0.1086	0.0729	2.6×10^{-7}
RSGH-2	random	10.4	64	0.1136	0.0813	2.5×10^{-7}
RSGH-3	random	15.5	62	0.1189	0.0833	2.4×10^{-7}
OSGH	ordered	15.5	130	0.1233	0.0889	4.8×10^{-7}

in the hydrogel. The behavior of the OSHG was similar to the RSHG, but the loss moduli decreased more than the RSHG at higher frequency. Even though the silica concentration is the same for these two composites, a difference was observed, especially in the loss modulus. From these master curves, we realize that the first two criteria for the application of TTS are satisfied. That is, (1) all adjacent curves overlap over a reasonable number of data points, and (2) the same values of the shift factor translate both the storage and the loss moduli.

A further condition that must be met for this system to obey TTS is that (3) the temperature dependence of the shift factors follows the Arrhenius relationship. Figure 9 shows temperature dependence of the shift factors for the PHG, the RSHG, and the OSHG. They are plotted against the reciprocal of temperature with respect to the reference temperature at 25 °C. E_a values were calculated from the slopes of these lines. Each of the samples exhibited a linear relationship, and it is obvious that the shift factors for all of these samples followed Arrhenius behavior. On the basis of these three criteria for the application of TTS, the PHG, the RSHG, and the OSHG all obey this principle.

In Figure 10, E_a values are plotted as a function of the silica content for the RSHG and OSHG. For the RSHG, E_a monotonically increases as the particle concentration increases. For the OSHG, E_a stays almost the same as the PHG. The RSHG with the same silica loading has significantly larger E_a than the OSHG. These samples were loaded to 10% shear strain, and the resultant stress relaxation was monitored (Figure 11a). The stress is normalized by the initial stress of each sample. Every sample exhibited the typical relaxation behavior of amorphous polymer. Normalized stress after 300 s as a function of the silica content is shown in Figure 11b. Their relaxation behaviors are similar to the tendency of E_a determined from the oscillatory shear experiment; the magnitude of the relaxation monotonically increases as the particle concentration increases for the RSHG, while the OSHG behaves very similar to the PHG.

4. Discussion

4.1. Interparticle Distance. Upon removal of excess ions from the system, the colloidal suspension undergoes a phase transition from a disordered state to either an FCC or BCC structure.[8,9] The colloidal array structure depends upon various factors, such as the sphere diameter, the sphere number density, the surface charge, the ionic strength, and the sample temperature.[32] To distinguish the crystal structure, an argon ion laser beam is commonly used to produce backscattered Kossel diffraction patterns.[9] In this study, however, we characterized it by the Bragg diffraction and compared it with the expected phase diagram for a colloidal suspension.

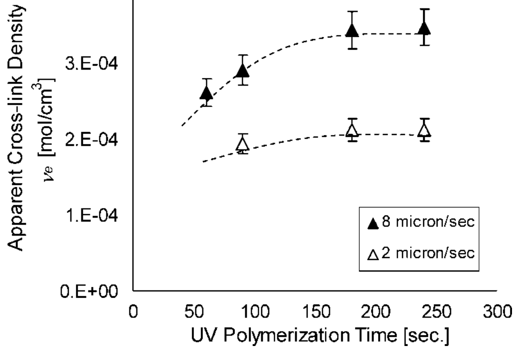

Figure 7. Apparent cross-link densities determined by stress−strain curves at different compression rate. The samples are the PHGs prepared by various UV polymerization times.

When colloidal crystals are in a cell, the crystals orient with their most densely packed planes parallel to the walls of the cell.[9] If the colloidal suspension takes an FCC structure, the most densely packed plane is (111), and the light is propagated along the [111] direction. Similarly, for a BCC structure, the light is propagated along either [110], [101], or [011]. On the basis of eqs 5 and 7, both crystal structures yielded an interparticle distance, d, of 223 nm. On the other hand, the interparticle distances calculated from eqs 6 and 8 were 232 nm for an FCC and 226 nm for a BCC structure. These values are determined solely from the atomic packing factor of the crystal structure at the given volume fraction and diameter of the silica particle and are regarded as theoretical interparticle distances. The fact that the experimentally determined interparticle distance from the Bragg diffraction, 223 nm, is very close to the theoretical interparticle distance for a BCC structure, 226 nm, suggests that the crystal lattice in the CCA-2 suspension and the OSHG consists mainly of a BCC structure.

This crystal structure is also confirmed by the phase diagram of colloidal suspensions predicted by Robbins et al.[33] using molecular dynamics calculations and verified experimentally by Monovoukas et al.[9] Robbins' phase diagram[33] (Figure 12) deals with a constant charge system of point particles interacting via a Yukawa potential. The x-axis of the phase diagram is the inverse Debye length times the average interparticle spacing, λ^*:

$$\lambda^* = \left(\frac{4\pi}{3\phi}\right)^{1/3} \kappa^* \tag{19}$$

where κ^* is the dimensionless inverse Debye length ($\kappa^* = \kappa R_p$) and ϕ is the volume fraction of particles. The y-axis of the diagram is a dimensionless temperature, T^*:

$$T^* = \frac{\exp(\lambda^*)}{\frac{1}{2}\left(\frac{R_p}{l}\right)\left(\frac{Q^2}{(1+\kappa^*)^2}\right)\exp(2\kappa^*)} \tag{20}$$

where l is the Bjerrum length ($l = e^2/4\pi\varepsilon kT$) and Q is the dimensionless surface charge density:

$$Q = \frac{eR_p}{\varepsilon kT}\sigma_0 \tag{21}$$

where σ_0 is the dimensional surface charge density. The relation between σ_0 and the surface potential, Φ_0, is given by solving the Poisson−Boltzmann equation[25] as

$$\sigma_0 = (8\varepsilon_r\varepsilon_0 kTc_{i0}^*)^{1/2} \sinh\left(\frac{ze\Phi_0}{2kT}\right) \tag{22}$$

In the CCA-2 suspension and the OSHG, $\lambda^* = 1.16$ and $T^* = 0.0094$. When we plot this point in the phase diagram, it

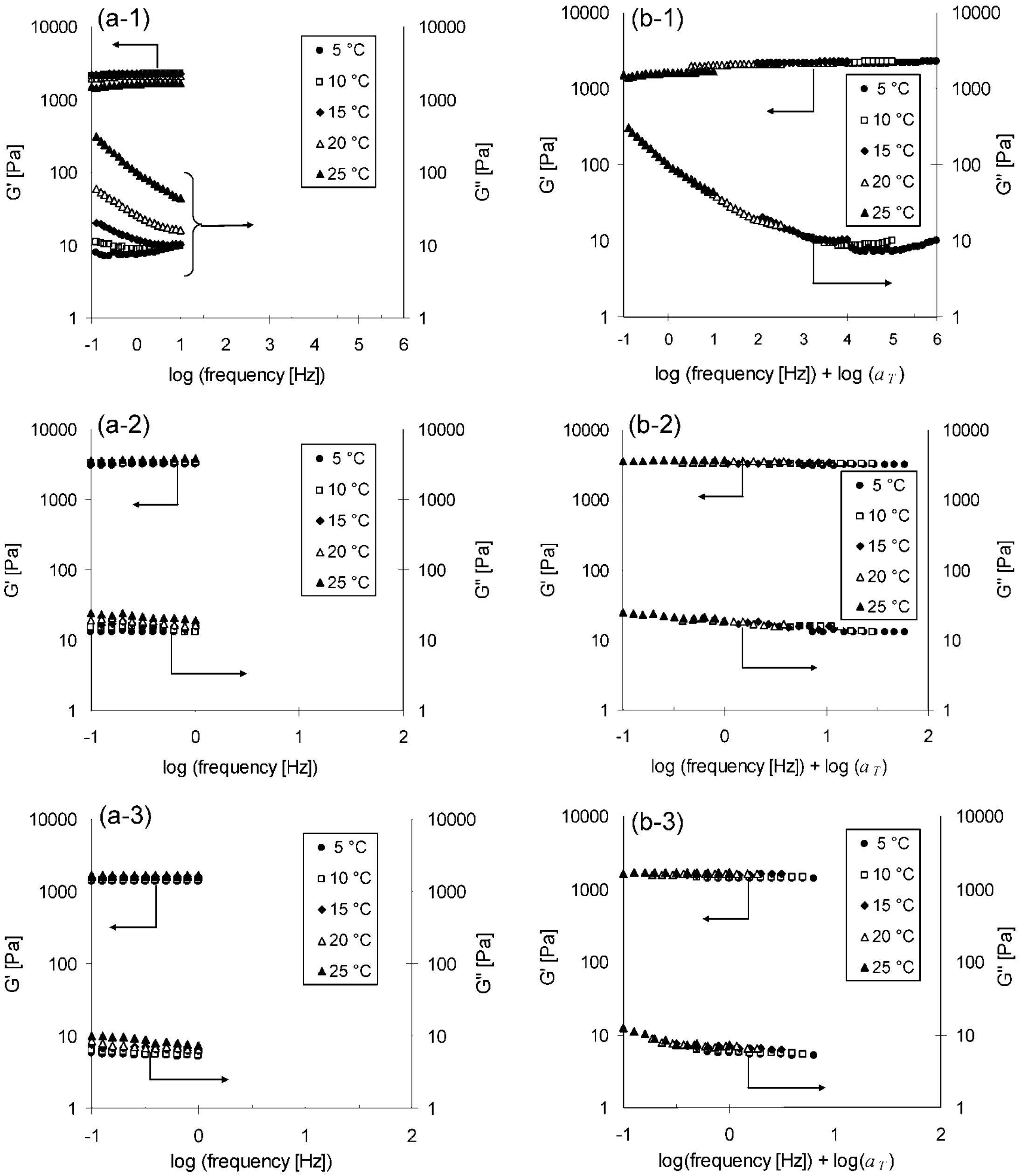

Figure 8. (a) Raw data of storage (G') and loss (G'') moduli for the PHG (a-1), the RSHG-3 (a-2), and the OSHG (a-3) at temperatures from 5 to 25 °C. (b) Master curves for the G' and G'' constructed at the reference temperature of 25 °C, using the same shift factor a_T for the G' and G''. For the RSHG-3 and the OSHG, silica concentrations are both 15.5 wt %.

falls into a BCC structure (Figure 12). This is consistent with the above argument using the theoretical atomic packing factors.

Note that the interparticle distance within the matrix is 203% larger than the distance between two centers of mass when two silica particles are in contact with each other. This is caused by the long-range electrostatic force at reduced counterion concentration forming the thicker Debye layer, which leads to the repulsion among charged particles. The UV−vis spectrophotometer, thus, enables us to easily evaluate the interparticle distance, *d*, of colloidal particles even after they are embedded in the polymeric matrix. This solved the first problem pointed out in the Introduction, which was how to evaluate the particle distribution.

Next, this interparticle distance will be compared with DLVO theory. Because the CCA is locked in the OSHG and the interparticle distance in water does not change upon polymerization,[13] the interparticle distance in the matrix should be explained by the balance of van der Waals attraction and the electrostatic repulsion between the charged surfaces of silica particles. This theory enables us to characterize not only the interparticle distance in the CCA but also the colloidal stability, which is derived by the barrier heights in the total interaction potential curve. From Figure 4, the separation distance between surfaces at which the secondary minimum appeared was longer for the OSHG than for the original suspension. The separation of surfaces at the secondary minimum was 110 nm for the OSHG. Taking into account the average diameter of the silica particles, 110 nm, we can calculate the interparticle distance, or the distance between two particles' center of mass, to be 220 nm. This value is comparable to 223 nm, the interparticle distance determined from Bragg diffraction, within our experimental error. This suggests that the driving force of the self-assembly into the crystal structure is, indeed, the balance of attractive and repulsive forces of charged particles and that the difference of the particle distribution between the OSHG and the RSHG is governed by only these forces.

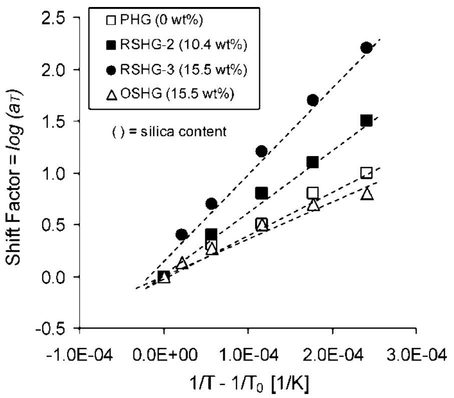

Figure 9. Arrhenius fit of shift factors for the PHG, the RSHG-2, the RSHG-3, and the OSHG. Silica content is indicated in the parentheses in the inset.

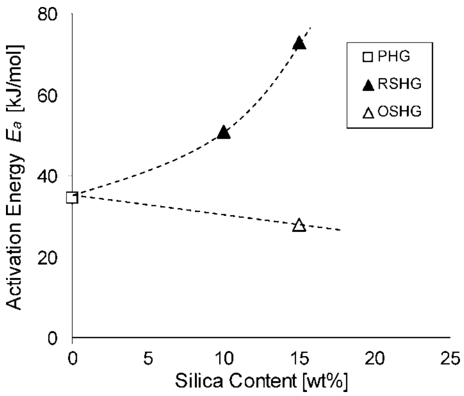

Figure 10. Activation energy associated with mechanical relaxation, E_a, as a function of the silica content in the polymeric matrix for the PHG, the RSHG, and the OSHG.

This solved the second problem of how to decouple the particle−matrix interaction and the particle distribution. In this system, the particle distribution was successfully controlled without changing the surface reactivity of particles or molecular weight of polymer chains. Taking advantage of the polymerized CCA, we were able to overcome the two challenges pointed out in the Introduction, and this sets the stage for the evaluation of the effect of the particle distribution upon the mechanical properties of the composites.

We will first attempt to verify two assumptions made in this section. The first assumption is that the electrical potential at the midpoint between the two surfaces is much smaller than the thermal energy. This condition is necessary for the linear superposition approximation to apply. From the interparticle distance determined by Bragg diffraction, we can calculate the electrical potential at the midpoint to be 5 mV. This corresponds to an electrical potential energy of 8×10^{-22} J and is less than 20% of the thermal energy. Therefore, this assumption is barely valid. The second assumption in DLVO theory is that the crystal structure is composed of a single crystal. Although the crystal structure of the OSHG looked homogeneous, this assumption of a single crystal is not perfectly true because the diffraction peak in Figure 2 has a finite value of half-width. Although these two assumptions are not completely valid, the fact that the interparticle distance determined by Bragg diffraction is well predicted by DLVO theory suggests that we can sufficiently determine the particle interaction through the linear superposition approximation and that the actual crystal structure can still be treated as a single BCC structure.

4.2. Apparent Cross-Link Density. The difference in the silica particle distribution resulted in a significant difference in the compressive moduli and the apparent cross-link densities. In the RSHG, the silica concentration does not have a big impact on modulus and apparent cross-link density. On the other hand, the OSHG has much larger compressive modulus and the apparent cross-link density at equivalent silica concentration than the RSHG. This suggests that the ordered distribution of particles within the matrix leads to larger effective contact area between the particle and the matrix. The silica particles in the RSHG tend to agglomerate, and the benefit of particle filling is significantly reduced. This difference in the apparent cross-link density between the RSHG and the OSHG suggests that the particle distribution in the matrix can change mechanical properties of the composite.

As opposed to the apparent cross-link density determined by the mechanical measurement, the swelling measurement did not provide a big difference between the RSHG and the OSHG. The reason for this phenomenon is considered to come from the physical interaction between the silica particle and the matrix polymer. The silanol groups on the silica surface can form a hydrogen bond with the amide groups of the pNIPAAm chain, and this contributes to a physical interaction. Therefore, the difference in the particle distribution should lead to a difference in the amount of the physical interactions between the polymer and the silica particles. From the above argument, the mechanical determination of the apparent cross-link density is more sensitive to the difference of the physical interactions in the sample. This is the reason why the stress−strain curves provided much larger difference between the RSHG and the OSHG than the swelling measurement (Figure 5).

4.3. Dynamic Mechanical Analysis. As described in section 3.3, all of the hydrogel composites in this study followed TTS. For the particle-filled polymer, this principle has been applied successfully for various other systems, such as carbon-black-filled styrene−butadiene−rubber[34] and silica-filled poly(vinyl acetate).[35] Ward[31] commented that this principle could not be applied to crystalline materials because of their complex thermal behavior. However, Faucher[36] argued that the principle could be applied to crystalline polymers if they are tested in the region in which their structure is maintained and under sufficiently low strain. Based on their discussion, the reason why one can apply this principle to our filled composite is that physical interaction between the silica surface and the polymer chains can act to maintain the composite structure and that our strain was not large enough to disrupt the structure.

The master curves of the PHG shown in Figure 8b represent a typical viscoelastic material. At lower frequency, the polymer chains have considerable time to respond to the mechanical input; therefore, it behaves more like a viscous material and the loss modulus increases. At higher frequency, on the other hand, the polymer chains do not have enough time to respond, and the material behaves as if it were elastic, which leads to smaller loss modulus. Incorporation of silica particles in the hydrogel significantly alters the composite's viscoelastic property. Both the RSHG and the OSHG are much more elastic, and the change in the loss modulus is decreased. This is quite reasonable because of the fact that they have elastic silica particles.

Comparing the RSHG and the OSHG provides the sole effect of particle distribution on the viscoelastic property of the composites. Although their master curves were similar to each other, the OSHG was less elastic than the RSHG as demonstrated by the larger increase in the loss modulus at lower frequency. This less elastic behavior of the OSHG is also demonstrated by the lower storage modulus, 1600 Pa, compared to 3600 Pa, the storage modulus of the RSHG. This can be explained by the agglomerated silica particles in the RSHG. In general, filler agglomeration within the polymeric matrix

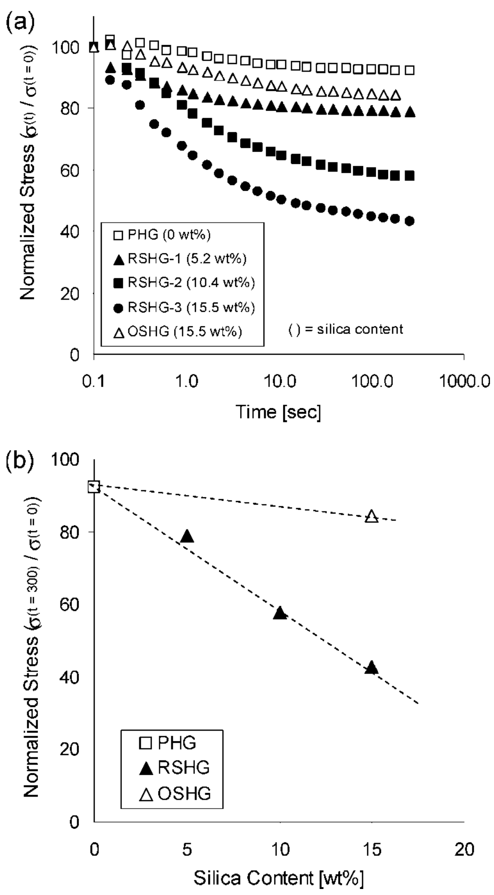

Figure 11. (a) Stress relaxation curves normalized by initial stress, $\sigma_{(t=0)}$, for the PHG, the RSHG, and the OSHG. Silica concentrations in the composites are indicated in parentheses in the inset. (b) Stress after 300 s normalized by $\sigma_{(t=0)}$ as a function of the silica content for the PHG, the RSHG, and the OSHG.

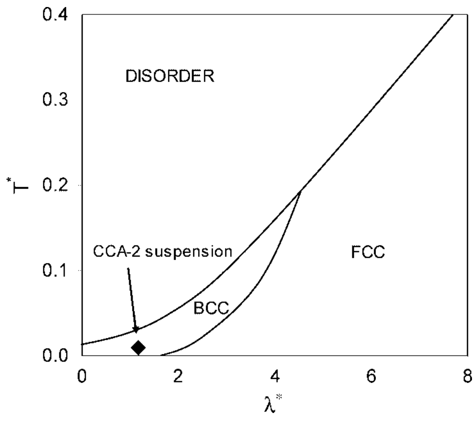

Figure 12. Phase diagram of colloidal suspensions in terms of the dimensionless temperature T^* and λ^*. The solid lines correspond to the order−disorder and BCC−FCC phase transitions according to the MD results of Robbins et al.[33] The CCA-2 suspension in this study falls into the BCC phase as shown in the diagram.

increases the stiffness of the composite, and better dispersion of fillers is believed to decrease the stiffness. This is common knowledge in the rubber industry, but in commercial practice the better dispersion of fillers is usually coupled with alteration of other factors, such as cleavage of the polymer chains and the particle−matrix interactions. The reduction of the elasticity observed in this study, however, is decoupled from these factors, and it is a pure effect of a better particle distribution.

The particles in the OSHG stay at their original positions before the polymerization, where they repel each other due to electrostatic repulsion. This should lead to minimum agglomeration of particles in the matrix. On the other hand, the particles in the aqueous suspension used for the RSHG are randomly distributed. It is quite natural that some silica particles are agglomerated in the original aqueous suspension because of the hydrogen bonding between silanol groups on the surface. As opposed to the OSHG, the silica particles in the RSHG are agglomerated and do not form a crystalline structure, which was confirmed by the noniridescence of the RSHG (Figure 1).

To investigate the significance of the particle distribution, we determined the apparent activation energy associated with the mechanical relaxation for these composites. The increase of E_a for the RSHG suggests that it is harder for this hydrogel to relax compared to the PHG. This tendency is enhanced as the silica loading increases in the RSHG. The increase of E_a, however, does not occur for the OSHG. The altered mobility of polymer chains in the vicinity of the particle surface induces changes in relaxation behaviors of the whole composite. The activation energy measurement in this study suggests that the presence of silica particles in the OSHG did not alter the mobility of polymer chains because the particles existed separately such that they did not perturb the polymer's mobility. We should realize that the composite's relaxation property is affected significantly by the distribution of silica particles and that the mobility of the silica-filled hydrogel is not inhibited so much if the particles are well distributed.

This analysis of the apparent activation energy was confirmed from the viewpoint of the stress relaxation behavior. The addition of silica particles in RSHG led to an increase in intensity of the stress relaxation (Figure 11b), and this tendency was also observed in other systems, such as carbon-black-filled[37] and Fe_2O_3-filled[38] polymer. The stress relaxation for the OSHG, on the other hand, was much smaller than the RSHG, which is reminiscent of the apparent activation energy data in Figure 10. This is also explained by the agglomeration of particles in the RSHG and the subsequent reduction of the composite's stress due to the breakage of the agglomerated particles in the hydrogel.

Summary

Silica-filled hydrogel composites were synthesized following previous reports by Asher et al.[10–12] Two distinct silica distributions were prepared within the matrix polymer, and the effect of the distribution was investigated. The crystal structure of the silica particles in the OSHG was determined to be a BCC structure from Bragg diffraction and the phase diagram. The interparticle distance in the OSHG obtained from Bragg diffraction was comparable to the one calculated from DLVO theory within our experimental error. This suggests that the difference of the particle distribution between the OSHG and the RSHG is controlled by only attractive and electrostatic repulsive forces among charged particles, without changing other factors in the system.

The apparent cross-link density was determined by both swelling and mechanical experiments, with the latter method being more sensitive to the physical interaction between the silica surface and the matrix polymer. The larger apparent cross-link density of the OSHG compared to the RSHG can be explained by the larger effective contact area between the silica particles and the matrix for the OSHG. Viscoelastic properties of the particle-filled hydrogels were characterized. We demonstrated that the relaxation behavior for the RSHG was different from the PHG and the OSHG. This can be explained by the agglomeration of particles in the RSHG and the reduction of the effective contact area between the particle and the matrix. This is consistent with the result of the apparent cross-link density analysis and also with the crystalline structure of the

OSHG, characterized by Bragg diffraction. These data provide a significant message that the particle distribution affects the mechanical property of the overall composite.

Acknowledgment. We thank Nippon Shokubai Co. Ltd. for their gift of the silica colloidal suspension. This work is supported by the Center on Polymer Interfaces and Macromolecular Assemblies (CPIMA), an NSF–MRSEC. M.Y. is grateful for support in the form of a fellowship from Bridgestone Corp. Many helpful discussions with Dr. Beinn O. V. Muir are gratefully acknowledged.

References and Notes

(1) Lipatov, Y. S. In *Polymer Reinforcement*; ChemTec Publishing: Toronto, Canada, 1995; p 63.
(2) Parkinson, D. *Br. J. Appl. Phys.* **1951**, *2*, 273–280.
(3) Wypych, G. In *Handbook of Fillers*, 2nd ed.; ChemTech Publishing: Toronto, Canada, 2000; p 257.
(4) Grunlan, J. C.; Gerberich, W. W.; Francis, L. F. *J. Mater. Res.* **1999**, *14*, 4132–4135.
(5) Yatsuyanagi, F.; Suzuki, N.; Ito, M.; Kaido, H. *Polymer* **2001**, *42*, 9523–9529.
(6) Shibayama, M.; Suda, J.; Karino, T.; Okabe, S.; Takehisa, T.; Haraguchi, K. *Macromolecules* **2004**, *37*, 9606–9612.
(7) Botti, A.; Pyckhout-Hintzen, W.; Urban, V.; Kohlbrecher, J.; Richter, D.; Straube, E. *Appl. Phys.* **2002**, *A74*, 513–515.
(8) Krieger, I. M.; O'Neill, F. M. *J. Am. Chem. Soc.* **1968**, *90*, 3114–3120.
(9) Monovoukas, Y.; Gast, A. *J. Colloid Interface Sci.* **1989**, *128*, 533–548.
(10) Weismann, J. M.; Sunkara, H. B.; Tse, A. S.; Asher, S. A. *Science* **1996**, *274*, 959–960.
(11) Holtz, J. H.; Holtz, J. S. W.; Munro, C. H.; Asher, S. A. *Anal. Chem.* **1998**, *70*, 780–791.
(12) Asher, S. A.; Holtz, J. H. *Nature (London)* **1997**, *389*, 829–832.
(13) Foulger, S. H.; Jiang, P.; Ying, Y.; Lattam, A. C.; Smith, D. W.; Ballato, J. M. *Langmuir* **2001**, *17*, 6023–6026.
(14) Bateman, J. B.; Weneck, E. J.; Eshler, D. C. *J. Colloid Sci.* **1959**, *14*, 308–329.
(15) Stokes, R. J.; Evans, D. F. In *Fundamentals of Interfacial Engineering*; Wiley-VCH: New York, 1997; (a) pp 145−156, (b) p 133.
(16) Verwey, E. J. W.; Overbeek, J. Th. G. In *Theory of the Stability of Lyophobic Colloids*; Elsevier: New York, 1948; p 143.
(17) Bray, J. C.; Merrill, E. W. *J. Appl. Polym. Sci.* **1973**, *17*, 3779–3794.
(18) Tasdalen, B.; Kayaman-Apohan, N.; Gueven, O.; Baysal, B. M. *Radiat. Phys. Chem.* **2004**, *69*, 303–310.
(19) Tayal, A.; Pai, V. B.; Khan, S. A. *Macromolecules* **1999**, *32*, 5567–5574.
(20) Painter, P. C.; Coleman, M. M. In *Fundamentals of Polymer Science*, 2nd ed.; Technomic Publishing Co.: Lancaster, PA, 1997; p 373.
(21) Fujishige, S. *Polym. J.* **1987**, *19*, 297–300.
(22) Tsubokawa, N.; Kimoto, T.; Koyama, K. *Colloid Polym. Sci.* **1993**, *271*, 940–946.
(23) Serizawa, T.; Wakita, K.; Kaneko, T.; Akashi, M. *J. Polym. Sci., Part A: Polym. Chem.* **2002**, *40*, 4228–4235.
(24) Gutowska, A.; Bae, Y. H.; Jacobs, H.; Feijen, J.; Kim, S. W. *Macromolecules* **1994**, *27*, 4167–4175.
(25) Sperling, L. H. In *Introduction to Physical Polymer Science*, 4th ed.; Wiley-Interscience: New York, 2006; p 473.
(26) Williams, M. L.; Landel, R. F.; Ferry, J. D. *J. Am. Chem. Soc.* **1955**, *77*, 3701–3707.
(27) Simon, P. P.; Ploehn, H. J. *J. Polym. Sci., Part B: Polym. Phys.* **1999**, *37*, 127–142.
(28) Akay, M.; Rollins, S. N. *Polymer* **1993**, *34*, 967–971.
(29) Kaplan, D.; Tschoegl, N. W. *Polym. Eng. Sci.* **1974**, *14*, 43–49.
(30) Shivakumar, E.; Das, C. K.; Segal, E.; Narkis, M. *Polymer* **2005**, *46*, 3363–3371.
(31) Ward, I. M. In *Mechanical Properties of Solid Polymer*, 2nd ed.; Wiley-Interscience: New York, 1983; Chapter 7.
(32) Rundquist, P. A.; Photinos, P.; Jagannathan, S.; Asher, S. A. *J. Chem. Phys.* **1989**, *91*, 4932–4941.
(33) Robbins, M. O.; Kremer, K.; Grest, G. S. *J. Chem. Phys.* **1988**, *88*, 3286–3312.
(34) Oono, R. *J. Polym. Sci., Polym. Phys. Ed.* **1974**, *12*, 1383–1394.
(35) Landry, C. J. T.; Coltrain, B. K.; Landry, M. R.; Fitzgerald, J. J.; Long, V. K. *Macromolecules* **1993**, *26*, 3702–3712.
(36) Faucher, J. A. *Trans. Soc. Rheol.* **1959**, *3*, 81–93.
(37) MacKenzie, C. I.; Scanlan, J. *Polymer* **1984**, *25*, 559–568.
(38) Djokovic, V.; Nedeljkovic, J. M. *Macromol. Rapid Commun.* **2000**, *21*, 994–997.

MA8003778